Chem

CellPress

Article

Intermediate-Temperature Anhydrous High Proton Conductivity Triggered by Dynamic Molecular Migration in Trinuclear Cluster Lattice

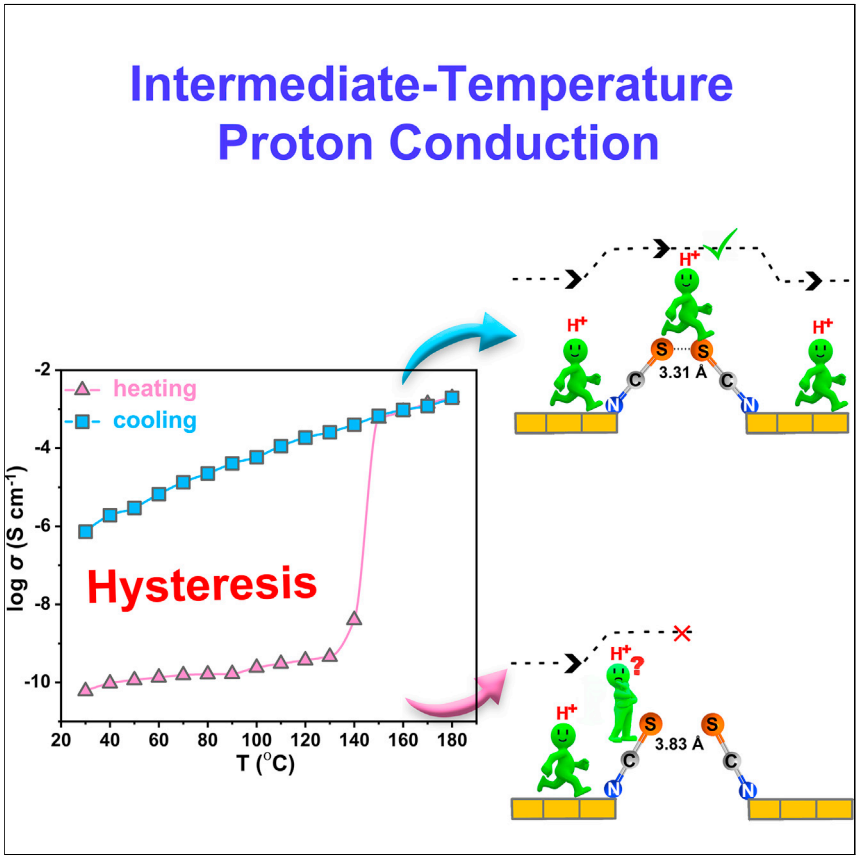

The hysteresis phenomenon of proton conductivity is triggered by a trinuclear cluster structural transformation with dynamic molecular migration, leading to high intermediate-temperature proton conductivity as a result of the supplementary highly efficient proton-transport channels ("SCN passageway").

Xiao-Min Li, Long-Zhang Dong, Jiang Liu, Wen-Xin Ji, Shun-Li Li, Ya-Qian Lan

liuj@njnu.edu.cn (J.L.)
yqlan@njnu.edu.cn (Y.-Q.L.)

HIGHLIGHTS

Conductivity "hysteresis" behavior is discovered

The SCN^- passageway can play a vital role in promoting efficient proton transfer

NNU-66a exhibits a very high proton conductivity of 1.94×10^{-3} S cm^{-1} at 180°C

Li et al., Chem 6, 2272–2282
September 10, 2020
https://doi.org/10.1016/j.chempr.2020.06.007

CellPress

Chem

Article

Intermediate-Temperature Anhydrous High Proton Conductivity Triggered by Dynamic Molecular Migration in Trinuclear Cluster Lattice

Xiao-Min Li,[1,3] Long-Zhang Dong,[1,3] Jiang Liu,[1,*] Wen-Xin Ji,[2] Shun-Li Li,[1] and Ya-Qian Lan[1,4,*]

SUMMARY

Building an efficient and uninterrupted hydrogen-bond network by visualized crystal-structure phase transformation to improve anhydrous proton conductivity and to elucidate the proton-transfer mechanism is desirable but rare. Here, we have discovered a proton conductivity "hysteresis" phenomenon triggered by an obvious structural transformation in which the dynamic molecular migration in a trinuclear cluster (NNU-66) results in the reorganization of the H-bond network. The cluster structure after transformation (NNU-66a) exhibits a remarkable proton conductivity of 1.94 × 10^{-3} S cm^{-1} and a superior performance durability of 24 h at 180°C. The peculiar "SCN^- passageway" in NNU-66a plays a vital role in building an effective hydrogen-bond network for fast proton transfer. Moreover, the corresponding density functional theory results indicate that the introduction of the SCN^- passageway dramatically lowers the energy required for proton hopping. Additionally, NNU-66a is further fabricated into a proton-exchange membrane and used in H_2/O_2 fuel cells.

INTRODUCTION

The proton-exchange membrane (PEM) is a core component of proton-exchange membrane fuel cells (PEMFCs) because it allows facile proton transport and determines the overall property of PEMFCs.[1–5] So far, Nafion is the most widely used commercial PEM because of its high proton conductivity of 10^{-2}–10^{-1} S cm^{-1} at 98% relative humidity.[6,7] However, Nafion strongly relies on water as the conductive medium, which results in high operating costs of the water management system[8] and impedes its wide utilization at a higher temperature range. Thus, intermediate-temperature (100°C–200°C) PEMFCs are the focus of researchers[9–11] because the higher operating temperature has the following advantages: (1) faster electrode reaction kinetics make it feasible to use other cheaper catalysts;[12] (2) the waste heat can be recycled for direct heating, steam reforming, and combined heat and power,[13] which achieves a greater energy utilization rate; and (3) the higher operating temperature can alleviate catalyst poisoning stemming from fuel impurity.[14] In particular, the operating temperature within the range of 150°C–180°C has become the most anticipated development direction. The lower temperature limit of 150°C is to reduce the affinity of carbon monoxide (CO) to avoid the serious performance damage caused by CO adsorption on platinum catalysts and increase the tolerance of electrocatalysts to CO to solve the problem of CO poisoning.[7,9,15–18] The upper temperature limit of 180°C is to avoid the degradation of membranes.[14] To date, two common intermediate-temperature proton-conducting materials—solid acids[19,20] and organic polymers[21,22]—have been investigated, but neither of them can maintain

The Bigger Picture

Intermediate-temperature (100°C–200°C) proton-exchange membranes with high proton conductivity and visualized proton-transfer pathways are very important for understanding and further developing the proton-transfer mechanism. However, most reported visualized crystalline proton conductive materials rely on water as the medium for proton transfer, so no efficient hydrogen-bond network can be formed to obtain high proton conductivity at intermediate temperatures in consideration of water evaporation. Here, we have synthesized a trinuclear cluster with high proton conductivity at intermediate temperature by forming a highly efficient and peculiar "SCN^- passageway" via structural transformation. Moreover, the structural transformation also results in conductivity hysteresis, which has not yet been reported in this area. Therefore, this work provides a unique idea for improving proton conductivity at intermediate temperatures.

performance under sustained operation because of their easy reduction and easy escape of acidic molecules, respectively.[23] Therefore, the development of a PEM simultaneously satisfying high performance and persistence at temperatures of 150°C–180°C is of great research value and significance.

Recently, metal-organic frameworks (MOFs) have made great contributions to the visualized exploration of hydrogen-bond networks[24–35] and the strategic improvement of proton conductivity[36–44] because of their definite structures and functional organic linkers. Currently, the reported high performance of MOF-based proton-conducting materials predominantly originates from external water, but these materials seriously lose water molecules as temperature increases (T > 70°C).[45] Thus, the continuous hydrogen-bond networks will be destroyed, leading to a dramatic decrease in conductivity, which is also the primary problem faced by MOFs as intermediate-temperature proton conductors. Theoretically, the key to overcoming this difficulty lies in the fact that the hydrogen-bond networks of materials will not be destroyed or even be able to form more effective proton-transport routes when the temperature rises. The important premise for achieving this strategy is generally that proton-conducting MOFs can alter their hydrogen-bond networks by virtue of large structural phase transitions with increasing temperature, thereby promoting their performance. However, the reported crystalline proton conductive materials, whether MOFs or covalent organic frameworks, have high-dimensional rigid structures, which makes it difficult to produce sufficiently large structural phase transitions even at higher temperatures. In contrast, a low-dimensional supramolecular structure stacked by hydrogen bonding, especially a zero-dimensional cluster, has the potential superiority of changing the hydrogen-bond network through thermally induced structural phase transition from three-dimensional directions. At present, materials with high intermediate-temperature proton conductivities attained from such a strategy of regulating H-bond networks by structural phase transition have not been reported.

Here, we synthesized a linear trinuclear cluster, $[Ni_3(NH_2\text{-trz})_6(SCN)_4(H_2O)_2](SCN)_2\cdot H_2O$ (denoted as **NNU-66**, NH_2-trz = 4-amino-1,2,4-triazole), and its isomorphic $[Fe_3(NH_2\text{-trz})_6(SCN)_4(H_2O)_2](SCN)_2\cdot H_2O$ (denoted as **NNU-67**) and $[Co_3(NH_2\text{-trz})_6(SCN)_4(H_2O)_2](SCN)_2\cdot H_2O$ (denoted as **NNU-68**) by a simple solvothermal reaction using cheap raw materials. Interestingly, we found a rarely seen phenomenon: the proton conductivity performance of these complexes abruptly increased when the temperature rose to a certain value. Moreover, when the temperature fell, their proton conductivity performance was obviously higher than that at the same temperature of the heating stage (i.e., generation of proton conductivity hysteresis), which indicates that a structural phase transition process favoring proton conduction could happen during the intermediate-temperature period (150°C to 180°C). Importantly, in order to confirm this speculation, we successfully captured the obvious dynamic molecular migrations in a nickel (Ni)-containing cluster structure lattice before and after the phase transition temperature by single-crystal X-ray diffraction (XRD) and clearly observed the variations in hydrogen-bond networks in this structural transformation process from **NNU-66** (before transformation) to **NNU-66a** (after transformation). Moreover, these three clusters after phase transformation showed high proton conductivities of 1.94×10^{-3} S cm^{-1} at 180°C (**NNU-66a**), 1×10^{-3} S cm^{-1} at 150°C (**NNU-67a**), and 9.43×10^{-4} S cm^{-1} at 160°C (**NNU-68a**), which surpass those of many representative anhydrous proton-conducting materials. To the best of our knowledge, this is the first crystalline material system to enrich the hydrogen-bond network through structural phase transition and then improve their performance of intermediate-temperature proton conduction. More significantly, we found that the dynamic migration of the SCN^- anion has a crucial role in improving proton conductivity because it provides an important "SCN^- passageway" in building a

[1]Jiangsu Collaborative Innovation Centre of Biomedical Functional Materials, Jiangsu Key Laboratory of New Power Batteries, School of Chemistry and Materials Science, Nanjing Normal University, Nanjing, Jiangsu 210023, P.R. China

[2]State Key Laboratory of High-Efficiency Coal Utilization and Green Chemical Engineering, Ningxia University, Yinchuan, Ningxia 750021, P.R. China

[3]These authors contributed equally

[4]Lead Contact

*Correspondence: liuj@njnu.edu.cn (J.L.), yqlan@njnu.edu.cn (Y.-Q.L.)

https://doi.org/10.1016/j.chempr.2020.06.007

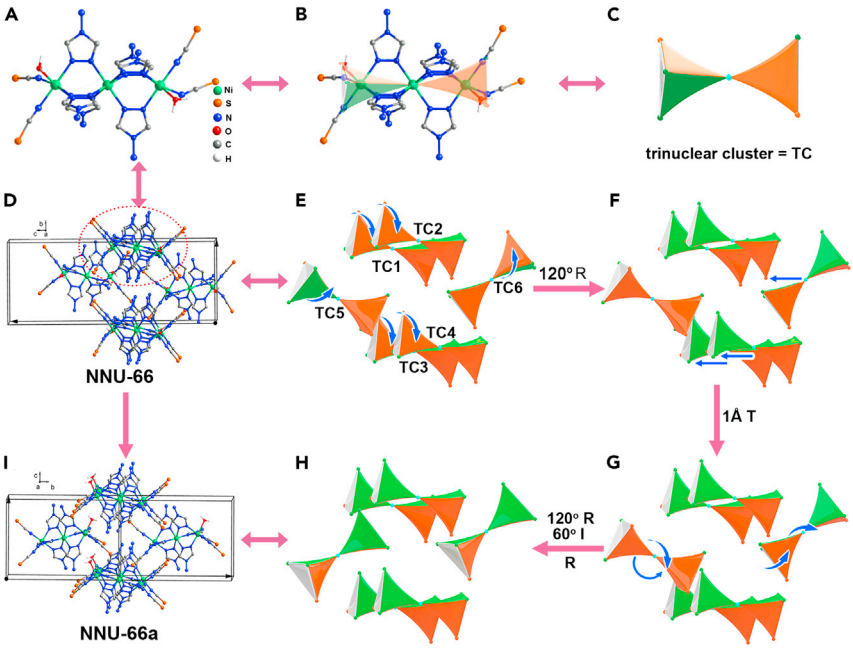

Figure 1. Schematic Representation of Single-Crystal-to-Single-Crystal Transformation

(A–C) In order to clearly show the process of crystal transformation, trinuclear clusters (A) (abbreviated as TC) are simplified. The two vertex-sharing tetrahedra represent a trinuclear cluster (B), in which one Ni, one O, and one N atom form an orange plane, one Ni and two N atoms form a green plane, and one O and two N atoms form a gray plane (C). See also Figure S2.

(D–I) Schematic representation of single-crystal-to-single-crystal transformation from **NNU-66** (D) to **NNU-66a** (I). TC1–TC6 represent six simplified trinuclear cluster models (E). The structural transformation experiences rotation (E and F), translation (F and G), and rotation and inclination (G and H). R, rotation; T, translation; I, inclination. See also Video S1.

highly efficient proton-transport route. It is worth noting that such a SCN^- passageway that can effectively improve the proton-transfer efficiency has not been reported before. On this basis, we further fabricated **NNU-66a** into a PEM and then used it in H_2/O_2 fuel cells.

RESULTS

Structure and Characterization

Single-crystal XRD analysis revealed that **NNU-66** crystallized in the $P2_12_12_1$ orthorhombic space group (Figure S1A; Tables S1 and S2). As shown in Figure S2, the crystal structure of **NNU-66** is composed of three Ni(II) ions, six NH_2-trz ligands, four coordinated SCN^- anions, two coordinated water molecules, two free SCN^- anions, and one lattice water molecule. Specifically, the central Ni(II) ion is surrounded by six N atoms from six NH_2-trz ligands, forming an octahedral geometry configuration and providing three triazole bridges for another two Ni(II) ions (Figure S3). Moreover, the octahedral coordination of two terminated Ni(II) ions is composed of three NH_2-trz, two terminated monodentate SCN^- ligands, and one H_2O molecule (Figure S4). The crystal structures of **NNU-67** and **NNU-68** are consistent with **NNU-66** except that they replace Ni with Fe and Co, respectively. When **NNU-66** (Figure 1D) was heated to the temperature range of 150°C–180°C, structural phase transition occurred (**NNU-66a**; Figure 1I). The specific structural transformation process adopting simplified models (two vertex-sharing tetrahedra represent a trinuclear cluster [TC]) is shown in Figures 1A–1C, and Video S1 shows this dynamic variation process of crystal structural transition (see the Supplemental Information). The left TC1–TC4

rotate anticlockwise by 120° with the gray bottom as the axis, whereas the left TC5 and the right TC6 rotate clockwise by 120° (Figures 1E and 1F). Then, TC3, TC4, and TC6 carry on translational motion of 1 Å (Figures 1F and 1G). Figures 1G and 1H show that TC5 experiences 120° clockwise rotation of the whole molecule with the gray bottom of the left tetrahedron as the axis and 60° inclination of the whole molecule with the right tetrahedron as the upward direction. Meanwhile, the orientation of TC6 is the same as that of TC5 after the rotation of the whole molecule, so the more ordered molecular structure can be obtained (Figures S5 and S6). Single-crystal XRD analysis after the structural transition indicated that **NNU-66a** crystallizes in the $P2_1/n$ monoclinic space group (Figure S1B; Tables S1 and S3). The crystal structure of **NNU-66a** is also composed of three Ni(II) ions, six NH_2-trz, four coordinated SCN^- anions, two coordinated water molecules, two free SCN^- anions, and one lattice water molecule (Figure S7). Similarly, the central Ni(II) ion is surrounded by six N atoms from six NH_2-trz ligands (Figure S8), and the other two Ni(II) ions are assembled with three NH_2-trz, two terminated monodentate SCN^- groups, and one H_2O molecule (Figure S9). It should be noted that the positions of free H_2O molecules and SCN^- anions in **NNU-66a** changed greatly in comparison with those in **NNU-66** (Figures S10 and S11).

Powder XRD (PXRD) measurements demonstrated that the patterns of the three complexes are well matched with the simulated one, confirming their high phase purities and similar crystalline structures (Figure S12). The scanning electron microscopy (SEM) images clearly show the morphologies of these clusters (Figures S13–S16). The results of elemental analysis of **NNU-66** and **NNU-66a** provided in the synthesis section of the Supplemental Information are consistent with those obtained from crystal structures. In order to further determine the elemental compositions of **NNU-66** and **NNU-66a**, we performed energy-dispersive X-ray (EDX) spectroscopy (Figures S17 and S18). The EDX spectra show that Ni, O, N, C, and S exist in **NNU-66** and **NNU-66a**, in which O comes from H_2O. The X-ray photoelectron spectroscopy (XPS) spectra shown in Figures S19 and S20 also reveal the presence of all elements (Ni, O, N, C, and S) and that O comes from the coordinated H_2O and free H_2O molecules in crystal lattices. Thermogravimetric analysis (TGA) of the three complexes indicated that their structures are stable before 180°C, 150°C, and 160°C (Figures S21A, S22A, and S23A). Moreover, combined with the TGA curves, the PXRD patterns of the heated samples show that they have enough high thermal stabilities to ensure the proton conductivity measurements (Figures S21B, S22B, and S23B). Meanwhile, the thermal stability of **NNU-66a** indicates that it remains structurally intact until 204°C (Figure S24).

Proton Conduction

Proton conductivity of the three complexes was measured by alternating-current (AC) impedance spectroscopy under continuous heating and anhydrous conditions (Figures 2A, S25A, and S26A). Combined with the thermogravimetric curves of these clusters, the upper temperature limits for proton-conductivity tests were set to 180°C, 150°C, and 160°C for **NNU-66**, **NNU-67**, and **NNU-68**, respectively. The Nyquist plots display two semicircles and a tail, among which the two arcs represent the bulk and grain boundary resistance, respectively, and the tail relates to the mobile ions blocked by the interface between the electrode and electrolyte (Figures S27–S29).[46] Moreover, we adopted bulk proton conductivities in this case, so we employed the intercepts along the x axes of higher frequency to gain the bulk resistances.[31] Interestingly, the conductivity performances of **NNU-66**, **NNU-67**, and **NNU-68** suddenly increased when the complexes were heated to a certain temperature: **NNU-66** jumped from 3.98×10^{-9} S cm^{-1} at 140°C to 5.8×10^{-4} S cm^{-1} at

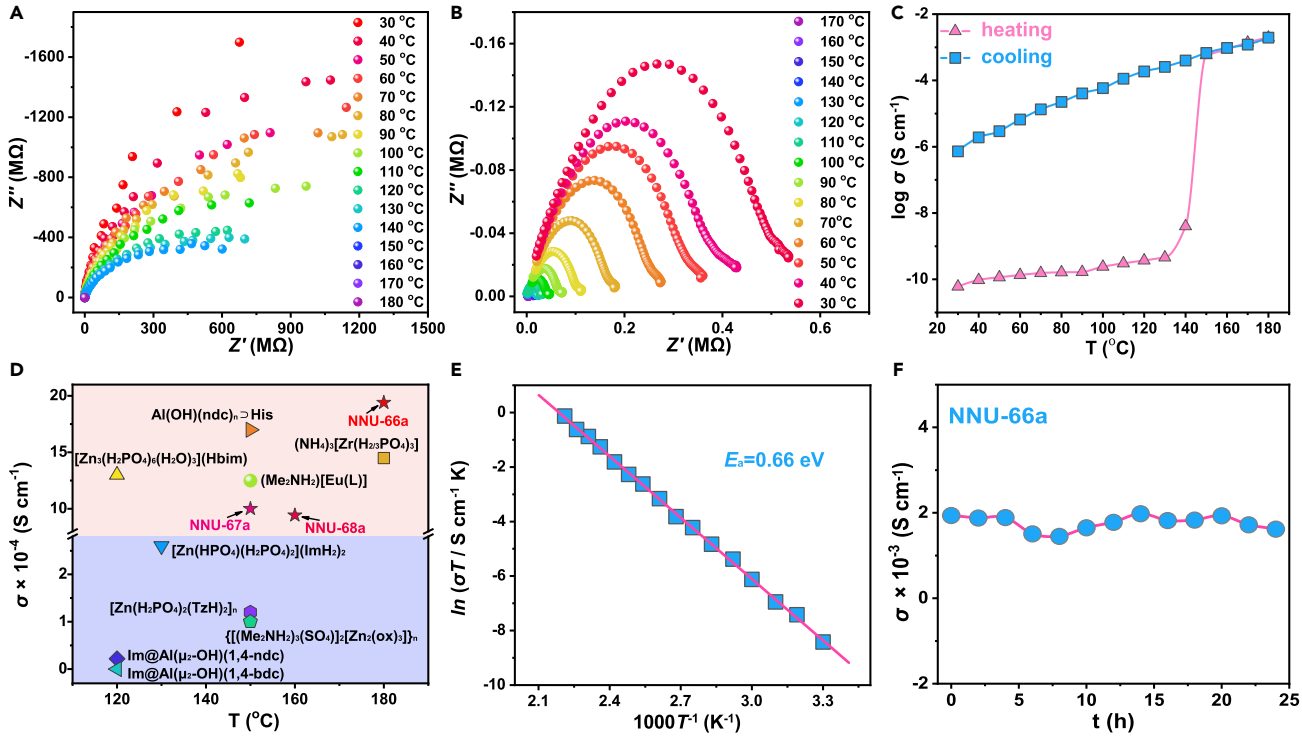

Figure 2. Proton Conductivity

(A and B) The Nyquist plots of **NNU-66** and **NNU-66a** at temperature ranges of 30°C–180°C (A) and 170°C–30°C (B).

(C) Temperature-dependent proton conductivities of **NNU-66** and **NNU-66a** (30°C–180°C).

(D) Comparison of the proton conductivity among **NNU-66a**, **NNU-67a**, **NNU-68a**, and some other representative materials.

(E) Arrhenius plot of **NNU-66a** at a temperature range of 30°C–180°C.

(F) Time-dependent proton conductivity of **NNU-66a** performed at 180°C.

150°C, **NNU-67** jumped from 1.59 × 10^{-7} S cm^{-1} at 130°C to 4.47 × 10^{-4} S cm^{-1} at 140°C, and **NNU-68** jumped from 3.90 × 10^{-8} S cm^{-1} at 150°C to 9.43 × 10^{-4} S cm^{-1} at 160°C (Figures 2C, S30, and S31). It is also worth mentioning that **NNU-66**, **NNU-67**, and **NNU-68** exhibited enhanced proton conductivities by 5, 3, and 4 orders of magnitude, respectively, after undergoing an abrupt increase in performance. Eventually, the conductivities of **NNU-66a** and **NNU-67a** reached 1.94 × 10^{-3} and 1 × 10^{-3} S cm^{-1} at 180°C and 150°C, respectively. Importantly, their highest performance values are comparable with those of the representative anhydrous proton-conducting materials shown in Figure 2D and Table S4, unveiling their potential for further application as PEMs. After the complexes reached the upper-limit temperatures, we further measured their proton conductivities after lowering the temperature (Figures 2B, S25B, and S26B). As shown in Figures 2B, S30, and S31, their performance values were evidently higher than those under the same temperatures of the heating period, implying that the phase-transition behavior accompanied by the formation of effective proton-transport paths occurred at elevated temperature.

In order to have a preliminary understanding of the proton-conducting mechanism, we calculated the activation energy (E_a) of the three samples after phase change during the cooling process (Figures 2E, S32, and S33). The values of the activation energy of **NNU-66a**, **NNU-67a**, and **NNU-68a** were 0.66, 0.71, and 0.66 eV, respectively, suggesting that the proton-transport process of the three complexes belongs to the vehicle mechanism. It can be concluded that the free H_2O molecules and SCN^- anions as proton carriers by

means of self-diffusion dominate proton transport between clusters, resulting in the vehicle mechanism.[36] Additionally, we carried out two heating-cooling cycles of proton-conductivity measurements of the Ni-containing complex with the temperature range of 30°C–180°C (Figure S34). As shown in Figure S35, **NNU-66** changed to **NNU-66a** in the first heating process, and in the subsequent temperature heating and cooling processes, the proton conductivities of **NNU-66a** were highly consistent with each other at the same temperatures, attesting to its structural stability in the measurement. It is well known that the sustainability of properties is a necessary condition for further application of materials on PEMFC. So, we performed the time-dependent measurements of the three complexes at their individual maximum temperature to verify the thermal stabilities of their proton conductivities. As shown in Figure 2F, the high proton conductivity of **NNU-66a** could be maintained for 24 h at 180°C without obvious loss, proving that **NNU-66a** has excellent durability in performance. Analogously, we found that the high proton conductivities of **NNU-67a** and **NNU-68a** also had good persistence (Figures S36 and S37), indicating that they possess indispensable prerequisites for further application. Meaningfully, the PXRD patterns showed that the peaks of **NNU-66** after undergoing proton-conductivity measurements were essentially consistent with the simulated peaks of heated crystal **NNU-66a** collected by single-crystal XRD, demonstrating that **NNU-66** undergoes phase transition to **NNU-66a** and keeps the structural integrity of **NNU-66a** during testing (Figure S38). Additionally, the infrared spectra of **NNU-66** after the test were in line with those of **NNU-66a**, validating the transformation of **NNU-66** to **NNU-66a** due to the increase in temperature in intermediate-temperature proton-conductivity measurements and that **NNU-66a** is structurally robust (Figure S39).

Electronic Conduction

To exclude the influence originating from electronic conduction to acquired conductivity, we also examined the electronic conductivity of **NNU-66** under identical temperature ranges (30°C–180°C) (Figure S40). Figure S41 intuitively illustrates the ultralow electronic conductivity of **NNU-66** during the heating process. On the basis of the comparison with proton conductivity at the same temperature, it shows that the electronic conductivity can be completely neglected because the proton conductivity is about 5 orders of magnitude higher than the electronic conductivity at 180°C, which leads to the conclusion that electronic conduction does not play a role in the obtained conductivity (Table S5). This means that the high conductivities under intermediate temperatures and anhydrous conditions derive from the intrinsic efficient proton transfer.

Mechanism of Proton Conduction

Achieving high proton conductivity is the most important goal in anhydrous proton conduction, where superior performance depends on the diversity of proton-hopping sites and routes along with fast proton mobility.[3,47] For the sake of systematically shedding light on the proton-transfer mechanisms, we comparatively analyzed the proton-transport processes in **NNU-66** and **NNU-66a** in detail via crystallography. During the testing process, as the temperature increased, **NNU-66** underwent phase transition and generated **NNU-66a**, which equipped **NNU-66a** with a supplementary SCN^- passageway, resulting in a highly efficient proton-transfer pathway (Figures 3A and 3B). This means that the proton-transfer pathways of **NNU-66a** contain effective zigzag-arranged SCN^- passageways composed of many "SCN bridges," which are built by each of the two adjacent SCN anions (Figure 3D), whereas the distance between SCN^- anions in **NNU-66** is too long to form such effective bridges for proton hopping (Figure 3C). Notably, the insertion of such "SCN bridges" efficiently shortens the distance of protons transfer in **NNU-66a**. Meanwhile, the SCN^- anion as a counterion can also promote the rapid movement

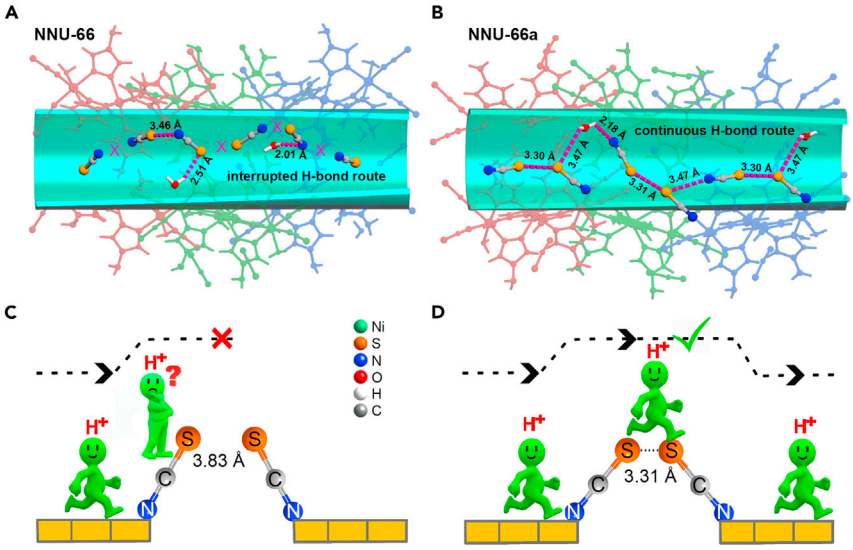

Figure 3. Proton-Transfer Mechanism

(A and B) Possible proton-transfer path of the SCN^- passageway in **NNU-66** (A) and **NNU-66a** (B). (C and D) Schematic representation of the proton transfer of the SCN bridge in **NNU-66** (C) and **NNU-66a** (D).

of H^+ [48,49] in the continuous SCN^- passageway and then further increase the efficiency of proton transport. Consequently, the proton conductivity of **NNU-66a** is greatly improved by the faster proton mobility and more diversified transmission paths, which are fundamentally caused by molecular rotation and movement.

DFT Calculations

Compared with **NNU-66**, **NNU-66a** has a faster proton-transport passageway for efficient proton transfer. In order to further understand the mechanism of proton conduction in **NNU-66a**, we applied DFT calculation by employing the models of SCN^- anions in **NNU-66** and **NNU-66a** extracted from their crystal structures. Results of the DFT calculation showed that the energy required for proton hopping with a distance of 3.83 Å between SCN^- anions of two adjacent TCs in **NNU-66** is 0.34 eV (Figure 4A). However, the distance between the SCN^- anions of two adjacent clusters becomes shorter in **NNU-66a** as a result of the molecular motions. As can be seen in Figure 4B, the energy required in **NNU-66a** for proton hopping between two similar adjacent SCN^- anions is almost negligible, which means that this process can be regarded as free movement. It is worth noting that the free movement is like self-diffusion. In other words, the SCN^- passageway of **NNU-66a** has been proved to not only be an efficient transport platform with almost zero energy consumption but also use the same self-diffusion mode to transfer protons, such as the vehicle mechanism of the experiment. Therefore, through the structural phase transition, **NNU-66a** can form a highly effective proton-transport H-bond network, thus obtaining high proton conductivity.

H_2/O_2 Fuel Cell

With the purpose of verifying the possibility of practical application, we fabricated **NNU-66a** into a membrane (Figures S42 and S43) and further assembled the membrane into a H_2/O_2 fuel cell (Figure 4C). Figure S44 shows the morphology and thickness of the **NNU-66a** membrane. In addition, the **NNU-66a** membrane has good thermal stability, which guarantees the intermediate-temperature test of fuel cells (Figure S45). The mechanical properties of the **NNU-66a** membrane are presented in Figure S46 and Table S6, which show 339.47 and 7.49 MPa for the elastic modulus and ultimate tensile strength,

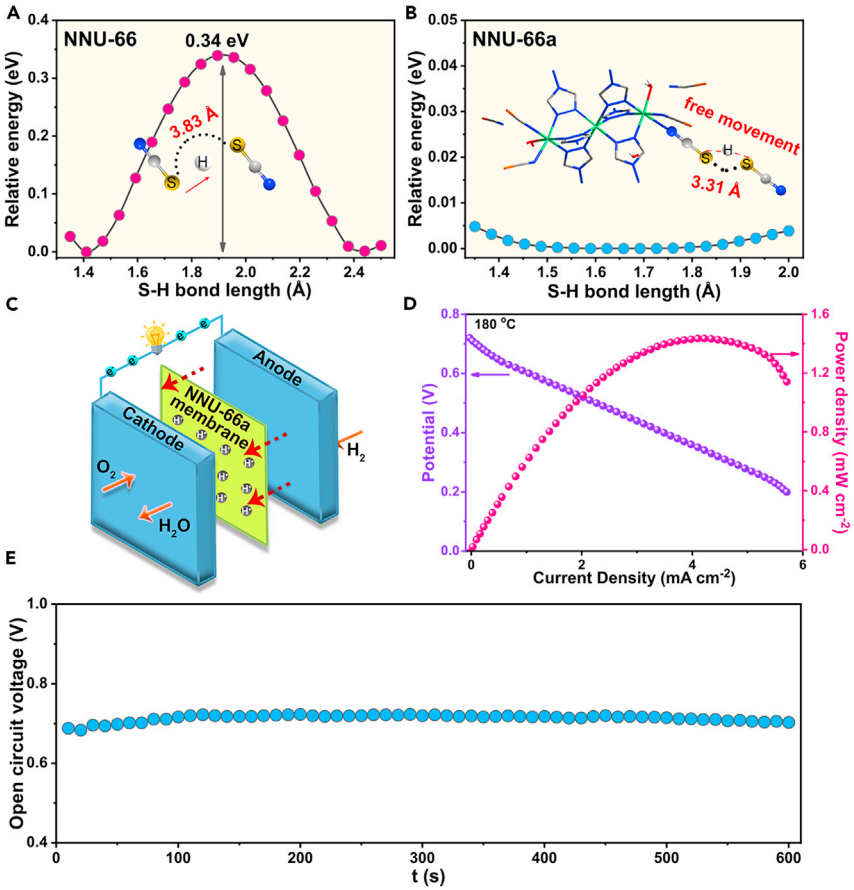

Figure 4. DFT Calculations and Performances of H_2/O_2 Fuel Cells

(A and B) DFT studies of the energy required for proton transport with SCN^- anions as the medium in **NNU-66** (A) and **NNU-66a** (B).

(C) Scheme of the PEMFC using the **NNU-66a** membrane as PEM.

(D) The performance of an H_2/O_2 fuel cell with the **NNU-66a** membrane as the electrolyte at 180°C. The purple and pink spheres represent current-voltage and current-power measurements, respectively.

(E) Plot of open-circuit voltage versus time at 180°C.

respectively. Furthermore, we explored the performance of the **NNU-66a** membrane and then concluded that the maximum open-circuit voltage and maximum power density are 0.72 V and 1.43 mW cm^{-2}, respectively, at 180°C (Figure 4D), which means that the **NNU-66a** membrane has the potential for further research in the field of intermediate-temperature PEMFCs. Additionally, as shown in Figure 4E, the performance of the H_2/O_2 fuel cell has good stability because of negligible degradation.

Conclusions

In summary, we have synthesized a TC model system used as an anhydrous proton conductor at intermediate temperature, and it exhibits a superior performance of 1.94×10^{-3} S cm^{-1} at 180°C, representing one of the highest values of reported intrinsic anhydrous proton-conducting materials. Furthermore, we manufactured the superior **NNU-66a** into a membrane and then used it in a H_2/O_2 fuel cell. Most importantly, we observed the proton conduction "hysteresis" caused by structural phase transition. Moreover, structural analysis of **NNU-66** and **NNU-66a** revealed that the efficiency including diversified and fast proton-hopping paths plays a significant role in inherent

proton conduction, in which our proposed SCN^- passageway is particularly important for fast proton transport. We propose a structural phase-transition strategy for regulating proton conductivity at intermediate temperatures, and it is important for the further development of proton conductors through visualized crystal structural change.

EXPERIMENTAL PROCEDURES

Resource Availability

Lead Contact

Further information and requests for resources should be directed to and will be fulfilled by the Lead Contact, Ya-Qian Lan (yqlan@njnu.edu.cn).

Materials Availability

This study did not generate new unique reagents.

Data and Code Availability

The accession numbers for the crystal structure CIF reported in this paper are CCDC: 1971816 and CCDC: 1971815 for **NNU-66** and **NNU-66a**, respectively.

Synthesis of $[Ni_3(NH_2\text{-trz})_6(SCN)_4(H_2O)_2](SCN)_2\cdot H_2O$ (NNU-66)

$NiSO_4\cdot 6H_2O$ (105 mg), NH_2-trz (67.5 mg), and NH_4SCN (61 mg) were dissolved in the mixed solution of CH_3OH (2.5 mL) and H_2O (5 mL). Subsequently, the solution was transferred into a 20 mL vial to be heated at 100°C for 72 h. When the reaction was complete, the mixture was filtered, and the filtrate was left to volatilize slowly. After a period of time, pale purple bulk crystals appeared in the filtrate, and these were cleaned with distilled water and naturally air dried. The final material was obtained. Yield: 63% based on $NiSO_4\cdot 6H_2O$. Elemental analysis calculated for **NNU-66** of $C_{18}H_{30}Ni_3N_{30}O_3S_6$ (%): C, 19.94; H, 2.77; N, 38.78; S, 17.73; found (%): C, 19.50; H, 2.76; N, 38.41; S, 17.23. FT-IR (KBr, cm^{-1}): 3,444 (m), 3,278 (m), 3,188 (w), 3,143 (w), 2,102 (s), 2,027 (s), 1,612 (s), 1,544 (s), 1,393 (m), 1,212 (s), 1,085 (s), 1,039 (s), 1,001 (s), 873 (m), 692 (m), 625 (s), 466 (m), 436 (m).

Synthesis of $[Fe_3(NH_2\text{-trz})_6(SCN)_4(H_2O)_2](SCN)_2\cdot H_2O$ (NNU-67)

$FeSO_4\cdot 7H_2O$ (110 mg), NH_2-trz (67.5 mg), and NH_4SCN (61 mg) were dissolved in a mixed solution of CH_3OH (2.5 mL) and H_2O (5 mL). Subsequently, the solution was transferred into a 20 mL vial to be heated at 100°C for 72 h. When the reaction was complete, the mixture was filtered, and the filtrate was left to volatilize slowly. After a period of time, green bulk crystals appeared in the filtrate, and these were cleaned with distilled water and naturally air dried. The final material was obtained.

Synthesis of $[Co_3(NH_2\text{-trz})_6(SCN)_4(H_2O)_2](SCN)_2\cdot H_2O$ (NNU-68)

$CoSO_4\cdot 7H_2O$ (112 mg), NH_2-trz (67.5 mg), and NH_4SCN (61 mg) were dissolved in a mixed solution of CH_3OH (2.5 mL) and H_2O (5 mL). Subsequently, the solution was transferred into a 20 mL vial to be heated at 100°C for 72 h. When the reaction was complete, the mixture was filtered, and the filtrate was left to volatilize slowly. After a period of time, green bulk crystals appeared in the filtrate, and these were cleaned with distilled water and naturally air dried. The final material was obtained.

Synthesis of NNU-66a

Crystal **NNU-66a** can be obtained by heating **NNU-66** to 180°C for several hours. Elemental analysis calculated for **NNU-66a** of $C_{18}H_{30}Ni_3N_{30}O_3S_6$ (%): C, 19.94; H, 2.77; N, 38.78; S, 17.73; found (%): C, 19.88; H, 2.85; N, 38.26; S, 17.89. FT-IR (KBr, cm^{-1}): 3,328 (w), 3,129 (m), 2,992 (w), 2,896 (m), 2,094 (s), 2,005 (s), 1,627 (s),

1,504 (s), 1,415 (m), 1,292 (s), 1,209 (m), 1,161 (s), 1,079 (s), 989 (s), 880 (s), 791 (w), 674 (s), 626 (s), 469 (w), 434 (w).

SUPPLEMENTAL INFORMATION

Supplemental Information can be found online at https://doi.org/10.1016/j.chempr.2020.06.007.

ACKNOWLEDGMENTS

This work was financially supported by the National Natural Science Foundation of China (21622104, 21701085, 21871141, 21871142, and 21901122), the National Science Foundation of Jiangsu Province of China (BK20171032), the Natural Science Research of Jiangsu Higher Education Institutions of China (17KJB150025 and 19KJB150011), a project funded by the China Postdoctoral Science Foundation (2018M630572 and 2019M651873), the Priority Academic Program Development of Jiangsu Higher Education Institutions, and the Foundation of Jiangsu Collaborative Innovation Center of Biomedical Functional Materials. We thank the staff of the BL17B beamline of the National Facility for Protein Science Shanghai at Shanghai Synchrotron Radiation Facility for helping with data collection. We thank Dr. Ling Zhao from China University of Geosciences for assisting with fuel cell measurements.

AUTHOR CONTRIBUTIONS

Conceptualization, Y.-Q.L. and J.L.; Methodology, X.-M.L. and L.-Z.D.; Investigation, J.L. and X.-M.L.; Formal Analysis, X.-M.L., L.-Z.D., and W.-X.J.; Writing – Original Draft, X.-M.L.; Writing – Review & Editing, J.L., S.-L.L., and X.-M.L.; Funding Acquisition, Y.-Q.L.; Supervision, Y.-Q.L. and J.L.

DECLARATION OF INTERESTS

The authors declare no competing interests.

Received: December 30, 2019
Revised: January 30, 2020
Accepted: June 2, 2020
Published: June 29, 2020

REFERENCES

1. Malavasi, L., Fisher, C.A., and Islam, M.S. (2010). Oxide-ion and proton conducting electrolyte materials for clean energy applications: structural and mechanistic features. Chem. Soc. Rev. *39*, 4370–4387.

2. Kreuer, K.D., Paddison, S.J., Spohr, E., and Schuster, M. (2004). Transport in proton conductors for fuel-cell applications: simulations, elementary reactions, and phenomenology. Chem. Rev. *104*, 4637–4678.

3. Zhang, H., and Shen, P.K. (2012). Recent development of polymer electrolyte membranes for fuel cells. Chem. Rev. *112*, 2780–2832.

4. Yoon, M., Suh, K., Natarajan, S., and Kim, K. (2013). Proton conduction in metal-organic frameworks and related modularly built porous solids. Angew. Chem. Int. Ed. *52*, 2688–2700.

5. Yamada, T., Otsubo, K., Makiura, R., and Kitagawa, H. (2013). Designer coordination polymers: dimensional crossover architectures and proton conduction. Chem. Soc. Rev. *42*, 6655–6669.

6. Mauritz, K.A., and Moore, R.B. (2004). State of understanding of Nafion. Chem. Rev. *104*, 4535–4585.

7. Paddison, S.J. (2003). Proton conduction mechanisms at low degrees of hydration in sulfonic acid-based polymer electrolyte membranes. Annu. Rev. Mater. Res. *33*, 289–319.

8. Chandan, A., Hattenberger, M., El-Kharouf, A., Du, S., Dhir, A., Self, V., Pollet, B.G., Ingram, A., and Bujalski, W. (2013). High temperature (HT) polymer electrolyte membrane fuel cells (PEMFC) - a review. J. Power Sources *231*, 264–278.

9. Li, Q., He, R., Jensen, J.O., and Bjerrum, N.J. (2003). Approaches and recent development of polymer electrolyte membranes for fuel cells operating above 100°C. Chem. Mater. *15*, 4896–4915.

10. Wang, Y., Chen, K.S., Mishler, J., Cho, S.C., and Adroher, X.C. (2011). A review of polymer electrolyte membrane fuel cells: technology, applications, and needs on fundamental research. Appl. Energy *88*, 981–1007.

11. Zhang, H., and Shen, P.K. (2012). Advances in the high performance polymer electrolyte membranes for fuel cells. Chem. Soc. Rev. *41*, 2382–2394.

12. Jaouen, F., Proietti, E., Lefèvre, M., Chenitz, R., Dodelet, J.-P., Wu, G., Chung, H.T., Johnston, C.M., and Zelenay, P. (2011). Recent advances in non-precious metal catalysis for oxygen-reduction reaction in polymer electrolyte fuel cells. Energy Environ. Sci. *4*, 114–130.

13. Rosli, R.E., Sulong, A.B., Daud, W.R.W., Zulkifley, M.A., Husaini, T., Rosli, M.I., Majlan, E.H., and Haque, M.A. (2017). A review of high-temperature proton exchange membrane fuel cell (HT-PEMFC) system. Int. J. Hydr. Energy *42*, 9293–9314.

14. Santra, A.K., and Goodman, D.W. (2002). Catalytic oxidation of CO by platinum group metals: from ultrahigh vacuum to elevated pressures. Electrochim. Acta *47*, 3595–3609.

15. Yang, C., Costamagna, P., Srinivasan, S., Benziger, J., and Bocarsly, A.B. (2001). Approaches and technical challenges to high temperature operation of proton exchange membrane fuel cells. J. Power Sources *103*, 1–9.

16. Pan, C., He, R., Li, Q., Jensen, J.O., Bjerrum, N.J., Hjulmand, H.A., and Jensen, A.B. (2005). Integration of high temperature PEM fuel cells with a methanol reformer. J. Power Sources *145*, 392–398.

17. Li, Q., He, R., Gao, J.-A., Jensen, J.O., and Bjerrum, N.J. (2003). The CO poisoning effect in PEMFCs operational at temperatures up to 200°C. J. Electrochem. Soc. *150*, A1599–A1605.

18. Kim, S.Y., Kim, S., and Park, M.J. (2010). Enhanced proton transport in nanostructured polymer electrolyte/ionic liquid membranes under water-free conditions. Nat. Commun. *1*, 88.

19. Boysen, D.A., Uda, T., Chisholm, C.R.I., and Haile, S.M. (2004). High-performance solid acid fuel cells through humidity stabilization. Science *303*, 68–70.

20. Haile, S.M., Boysen, D.A., Chisholm, C.R.I., and Merle, R.B. (2001). Solid acids as fuel cell electrolytes. Nature *410*, 910–913.

21. Asensio, J.A., Sánchez, E.M., and Gómez-Romero, P. (2010). Proton-conducting membranes based on benzimidazole polymers for high-temperature PEM fuel cells. A chemical quest. Chem. Soc. Rev. *39*, 3210–3239.

22. Zhang, J., Tang, Y., Song, C., and Zhang, J. (2007). Polybenzimidazole-membrane-based PEM fuel cell in the temperature range of 120–200 °C. J. Power Sources *172*, 163–171.

23. Gui, D., Dai, X., Tao, Z., Zheng, T., Wang, X., Silver, M.A., Shu, J., Chen, L., Wang, Y., Zhang, T., et al. (2018). Unique proton transportation pathway in a robust inorganic coordination polymer leading to intrinsically high and sustainable anhydrous proton conductivity. J. Am. Chem. Soc. *140*, 6146–6155.

24. Pili, S., Argent, S.P., Morris, C.G., Rought, P., García-Sakai, V., Silverwood, I.P., Easun, T.L., Li, M., Warren, M.R., Murray, C.A., et al. (2016). Proton conduction in a phosphonate-based metal–organic framework mediated by intrinsic "free diffusion inside a sphere". J. Am. Chem. Soc. *138*, 6352–6355.

25. Ōkawa, H., Sadakiyo, M., Yamada, T., Maesato, M., Ohba, M., and Kitagawa, H. (2013). Proton-conductive magnetic metal–organic frameworks, {NR3(CH2COOH)}[M(a)(II) M(b)(III)(ox)3]: effect of carboxyl residue upon proton conduction. J. Am. Chem. Soc. *135*, 2256–2262.

26. Sen, S., Nair, N.N., Yamada, T., Kitagawa, H., and Bharadwaj, P.K. (2012). High proton conductivity by a metal–organic framework incorporating Zn_8O clusters with aligned imidazolium groups decorating the channels. J. Am. Chem. Soc. *134*, 19432–19437.

27. Sadakiyo, M., Okawa, H., Shigematsu, A., Ohba, M., Yamada, T., and Kitagawa, H. (2012). Promotion of low-humidity proton conduction by controlling hydrophilicity in layered metal-organic frameworks. J. Am. Chem. Soc. *134*, 5472–5475.

28. Lim, D.W., Sadakiyo, M., and Kitagawa, H. (2019). Proton transfer in hydrogen-bonded degenerate systems of water and ammonia in metal–organic frameworks. Chem. Sci. *10*, 16–33.

29. Jeong, N.C., Samanta, B., Lee, C.Y., Farha, O.K., and Hupp, J.T. (2012). Coordination-chemistry control of proton conductivity in the iconic metal-organic framework material HKUST-1. J. Am. Chem. Soc. *134*, 51–54.

30. Bazaga-García, M., Colodrero, R.M., Papadaki, M., Garczarek, P., Zoń, J., Olivera-Pastor, P., Losilla, E.R., León-Reina, L., Aranda, M.A., Choquesillo-Lazarte, D., et al. (2014). Guest molecule-responsive functional calcium phosphonate frameworks for tuned proton conductivity. J. Am. Chem. Soc. *136*, 5731–5739.

31. Mileo, P.G.M., Adil, K., Davis, L., Cadiau, A., Belmabkhout, Y., Aggarwal, H., Maurin, G., Eddaoudi, M., and Devautour-Vinot, S. (2018). Achieving superprotonic conduction with a 2D fluorinated metal–organic framework. J. Am. Chem. Soc. *140*, 13156–13160.

32. Park, S.S., Rieth, A.J., Hendon, C.H., and Dincă, M. (2018). Selective vapor pressure dependent proton transport in a metal–organic framework with two distinct hydrophilic pores. J. Am. Chem. Soc. *140*, 2016–2019.

33. Zhang, F.M., Dong, L.Z., Qin, J.S., Guan, W., Liu, J., Li, S.L., Lu, M., Lan, Y.Q., Su, Z.M., and Zhou, H.C. (2017). Effect of imidazole arrangements on proton-conductivity in metal–organic frameworks. J. Am. Chem. Soc. *139*, 6183–6189.

34. Wang, S., Wahiduzzaman, M., Davis, L., Tissot, A., Shepard, W., Marrot, J., Martineau-Corcos, C., Hamdane, D., Maurin, G., Devautour-Vinot, S., et al. (2018). A robust zirconium amino acid metal-organic framework for proton conduction. Nat. Commun. *9*, 4937.

35. Gui, D., Duan, W., Shu, J., Zhai, F., Wang, N., Wang, X., Xie, J., Li, H., Chen, L., Diwu, J., et al. (2019). Persistent superprotonic conductivity in the order of 10^{-1} $S \cdot cm^{-1}$ achieved through thermally induced structural transformation of a uranyl coordination polymer. CCS Chem *1*, 197–206.

36. Ye, Y., Guo, W., Wang, L., Li, Z., Song, Z., Chen, J., Zhang, Z., Xiang, S., and Chen, B. (2017). Straightforward loading of imidazole molecules into metal-organic framework for high proton conduction. J. Am. Chem. Soc. *139*, 15604–15607.

37. Taylor, J.M., Dekura, S., Ikeda, R., and Kitagawa, H. (2015). Defect control to enhance proton conductivity in a metal–organic framework. Chem. Mater. *27*, 2286–2289.

38. Kim, S., Joarder, B., Hurd, J.A., Zhang, J., Dawson, K.W., Gelfand, B.S., Wong, N.E., and Shimizu, G.K.H. (2018). Achieving superprotonic conduction in metal–organic frameworks through iterative design advances. J. Am. Chem. Soc. *140*, 1077–1082.

39. Wong, N.E., Ramaswamy, P., Lee, A.S., Gelfand, B.S., Bladek, K.J., Taylor, J.M., Spasyuk, D.M., and Shimizu, G.K.H. (2017). Tuning intrinsic and extrinsic proton conduction in metal-organic frameworks by the lanthanide contraction. J. Am. Chem. Soc. *139*, 14676–14683.

40. Phang, W.J., Lee, W.R., Yoo, K., Ryu, D.W., Kim, B., and Hong, C.S. (2014). PH-dependent proton conducting behavior in a metal-organic framework material. Angew. Chem. Int. Ed. *53*, 8383–8387.

41. Phang, W.J., Jo, H., Lee, W.R., Song, J.H., Yoo, K., Kim, B., and Hong, C.S. (2015). Superprotonic conductivity of a UiO-66 framework functionalized with sulfonic acid groups by facile postsynthetic oxidation. Angew. Chem. Int. Ed. *54*, 5142–5146.

42. Liu, Y., Yang, X., Miao, J., Tang, Q., Liu, S., Shi, Z., and Liu, S. (2014). Polyoxometalate-functionalized metal-organic frameworks with improved water retention and uniform proton-conducting pathways in three orthogonal directions. Chem. Commun. *50*, 10023–10026.

43. Li, X.-M., Liu, J., Zhao, C., Zhou, J.-L., Zhao, L., Li, S.-L., and Lan, Y.-Q. (2019). Strategic hierarchical improvement of superprotonic conductivity in a stable metal-organic framework system. J. Mater. Chem. A *7*, 25165–25171.

44. Li, W.-H., Deng, W.-H., Wang, G.-E., and Xu, G. (2020). Conductive MOFs. Energychem *2*, 100029.

45. Qin, L., Yu, Y.Z., Liao, P.Q., Xue, W., Zheng, Z., Chen, X.M., and Zheng, Y.Z. (2016). A "molecular water pipe": a giant tubular cluster {Dy72} exhibits fast proton transport and slow magnetic relaxation. Adv. Mater. *28*, 10772–10779.

46. Ponomareva, V.G., Kovalenko, K.A., Chupakhin, A.P., Dybtsev, D.N., Shutova, E.S., and Fedin, V.P. (2012). Imparting high proton conductivity to a metal–organic framework material by controlled acid impregnation. J. Am. Chem. Soc. *134*, 15640–15643.

47. Yoshida, Y., Fujie, K., Lim, D.W., Ikeda, R., and Kitagawa, H. (2019). Superionic conduction over a wide temperature range in a metal-organic framework impregnated with ionic liquids. Angew. Chem. Int. Ed. *58*, 10909–10913.

48. West, I.C., and Mitchell, P. (1974). Proton/sodium ion antiport in Escherichia coli. Biochem. J. *144*, 87–90.

49. Srivastava, N., Chandra, A., and Chandra, S. (1995). Dense branched growth of (SCN)x and ion transport in the poly(ethyleneoxide) NH4SCN polymer electrolyte. Phys. Rev. B Condens. Matter *52*, 225–230.